Materials Today Energy 46 (2024) 101715

Contents lists available at ScienceDirect

Materials Today Energy

journal homepage: www.journals.elsevier.com/materials-today-energy/

Tuning the bandgap without compromising efficiency: Ambient solution processing of Ge-alloyed $(Ag,Cu)_2Zn(Sn,Ge)(S,Se)_4$ kesterite thin-film solar cells

Romain Scaffidi [a,b,c,d,*], Yuancai Gong [e], Alex Jimenez-Arguijo [e], Axel Gon Medaille [e], Sunil Suresh [a,b,c], Guy Brammertz [a,b,c], Sergio Giraldo [e], Joaquim Puigdollers [e], Denis Flandre [d], Bart Vermang [a,b,c], Edgardo Saucedo [e]

[a] imo-imomec, Hasselt University, Martelarenlaan 42, Hasselt, 3500, Belgium
[b] imo-imomec, imec, Thor Park 8320, Genk, 3600, Belgium
[c] imo-imomec, EnergyVille, Thor Park 8320, Genk, 3600, Belgium
[d] ICTEAM, Université Catholique de Louvain, Place du Levant 3, Louvain-la-Neuve, 1348, Belgium
[e] Electronic Engineering Department, Universitat Politècnica de Catalunya, Av Eduard Maristany 10–14, Barcelona, 08019, Spain

ARTICLE INFO

Keywords:
Photovoltaics
Kesterite
Bandgap tuning
Ge alloying
Solution processing

ABSTRACT

The photovoltaic sector currently experiences a growing demand for deeply-integrated technologies in agriculture, buildings, vehicles, among others. Kesterite compounds provide a versatile solution through their tunable bandgap via isovalent alloying. However, this should be done while preserving material opto-electronic quality and device performance, which is an unresolved challenge. Indeed, tuning the bandgap of kesterites must ensure low crystalline disorder to counteract the associated open-circuit voltage (V_{oc}) losses when used in solar cells. To achieve this goal, this work introduces a simple molecular ink recipe realized in ambient air to process single-phase high-quality Ag,Gealloyed kesterite absorbers. By varying the Ge content from 0 to 100 %, the absorber bandgap covers the range from 1.15 to 1.5 eV, in which the Urbach energy remains close to 20 meV and promisingly low V_{oc} deficits are observed. In particular, the champion efficiency of 12.1 % obtained with 40 % Ge breaks the record for Ge-alloyed kesterites with a 1.2 eV bandgap by remarkably reaching 62 % of the Shockley-Queisser limit for V_{oc}. This study demonstrates a promising strategy to solve the issue of large band tailing and low opto-electronic quality in widebandgap kesterites while establishing a foundation for solution-processed kesterite solar cells with tunable bandgap and promising performance.

1. Introduction

Photovoltaics (PV) is now playing a major role in the transition towards more sustainable electricity production, with more than 1 TW cumulative capacity already installed and record exponential growth in the past years for solar panels primarily made of Silicon. However, the PV industry is now expanding to new markets and applications where mechanical flexibility, low weight, tunable colour and opacity as well as tolerance to different light conditions are required, e.g. building- and vehicle-integrated photovoltaics (BIPV and VIPV), agrivoltaics (agriPV), indoor PV (IPV), …

Thin-film solar cells meet most of those requirements through their versatile design and material-sober architectures. In particular, the kesterite material family historically based on $Cu2ZnSn(S,Se)_4$ (CZTSSe) has emerged as a promising solution for single-junction PV absorbers relying on non-toxic and abundant elements, the bandgap of which can also be tuned in a range well-adapted to tandem PV structures [1–6]. Yet, those inorganic compounds are still facing major hurdles to become a viable alternative to commercially established $Cu(In,Ga)Se_2$ and CdTe technologies, summarized herein as three main challenges. First, the control of crystalline phase and composition in a homogeneous and reproducible fashion is a long-standing issue for kesterites [3,7,8], especially when deposited via physi-cal processes [4]. Second, the numerous point defects and high crystalline disorder existing in the kesterite lattice are considered the main culprits for their still too high open-circuit voltage (V_{oc}) deficits [3,7,8,8–11]. Third, precisely

* Corresponding author. imo-imomec, Hasselt University, Martelarenlaan 42, Hasselt, 3500, Belgium.
E-mail address: romain.scaffidi@imec.be (R. Scaffidi).

https://doi.org/10.1016/j.mtener.2024.101715
Received 5 September 2024; Received in revised form 25 September 2024; Accepted 11 October 2024
Available online 12 October 2024

controlling the kesterite absorber bandgap, e.g. via the S-Se ratio, is usually complex and realized at the expense of opto-electronic quality [8,12–15].

Fortunately, recent studies have investigated solutions addressing those two first challenges, which permitted kesterite solar cell power conversion efficiency (PCE) to reach beyond 14 % after more than a decade of status quo [16–19]. Indeed, such performance improvements were enabled by the transition towards more costeffective molecular ink routes which arguably allow finer control of reaction mechanisms and kinetics as well as phase formation [17–23]. In parallel, it facilitates the alloying of alternative metallic cations, which has been key to overcome the defective and disordered character of intrinsic kesterites [3,24,25], e.g. replacing Cu by Li and Ag [17,18,20,26], Zn by Cd [19,27,28], and Sn by Ge [4,19,22,29–38], among others. However, the third challenge of varying the kesterite bandgap while preserving its quality as a PV absorber remains largely unsolved. The solution may reside in the isovalent alloying of Ge to replace Sn, so as to widen the kesterite absorber bandgap for tandem or indoor PV applications [1,3–5], or to realize bandgap gradient designs known to typically boost the device efficiency [8,14,29,30,39–43]. Still, most studies up to this day have focused on Ge contents below 40 % [4], with many of them highlighting the difficulty to reach higher Ge incorporation.

Therefore, in this work, we aim at building on and extending those recent investigations about Ge alloying to simultaneously solve those 3 critical challenges faced by kesterite solar cells. More precisely, we develop a molecular ink solution process in ambient air that incorporates beyond 40 % of Ge to control the bandgap of high-quality Ag-alloyed $(Ag,Cu)_2Zn(Sn,Ge)(S,Se)_4$ (ACZTGSSe) kesterite thin films in a wide range. By a simple substitution to Sn directly in the precursor solution, Ge is properly integrated into single-phase polycrystalline kesterite absorbers with flexible bandgap tuning from 1.15 to 1.5 eV for 0–100 % Ge. The incorporation of Ge and associated bandgap widening do not compromise opto-electronic quality since benign Urbach tail coupled to low V_{oc} deficit is observed regardless of the bandgap. In particular, the champion device containing 40 % Ge reaches a remarkable 12.1 % efficiency without anti-reflective coating (ARC) and 62 % of the detailed balance limit for V_{oc}, which sets a new record for Ge-alloyed kesterites with a bandgap of 1.2 eV. The outstanding resilience of Urbach energy to larger bandgaps demonstrated in this study is an important milestone in the development of high-quality kesterite absorbers processed via cheap solution-based routes and adapted to tandem and indoor PV applications, among others. This shall require the optimization of heterojunction (HJ) band alignment and detrimental electronic defects for the highest Ge contents.

2. Materials and methods

The device fabrication process is schematically illustrated in Fig. 1 and inspired from a previous work [17]. The precursor solutions are prepared following the same molecular ink chemical route in ambient air. First, the CuCl, AgCl, $SnCl_4$, $GeCl_4$ and $Zn(CH_3CO_2)_2$ precursors are mixed with Thiourea (TU) in Dimethyl Formamide (DMF) solvent with a molarity of TU/(Ag + Cu + Zn + Sn + Ge) = 1.8 M. The ratios of $SnCl_4$ and $GeCl_4$ are adapted to cover the following target compositions: Ge/(Ge + Sn) = 0, 40, 60, 80 and 100 % with the corresponding device batches designated 0Ge, 40Ge, 60Ge, 80Ge and 100Ge in the text. The other compositional ratios are kept fixed at Ag/(Ag + Cu) = 0.15, (Ag + Cu)/(Zn + Sn + Ge) = 0.80 and Zn/(Sn + Ge) = 1.10. Before proceeding to the next steps, between 50 μL and 100 μL of 37 % concentrated HCl was added to the precursor solutions of 60Ge, 80Ge and 100Ge to achieve full dissolution. The final filtered precursor solution, clear and stable for weeks, is subsequently spin-coated on cleaned SLG/Mo substrates for 60 s at 3000 rpm, then placed on a hotplate for 3 min at a temperature of 340 °C also in ambient environment. This sequence is repeated 8 times with the objective to obtain 1 μm-thick precursor films. The precursor films are placed inside semi-closed graphite boxes with 400 mg Se pellets in a tube furnace filled with Ar at a pressure around 500 mbar. The selenization then starts by ramping up at 20 °C/min to reach 560 °C, remains at high temperature for 15 min before naturally cooling down. The 50 nm CdS buffer layer is deposited by chemical bath, followed by RF sputtering of 40 nm i-ZnO and 150 nm ITO window layers and finally thermal evaporation of 500 nm-thick Ag grid to complete the 0.23 cm^2 solar cells. No ARC is deposited on the studied samples. The details for experimental characterization are provided in

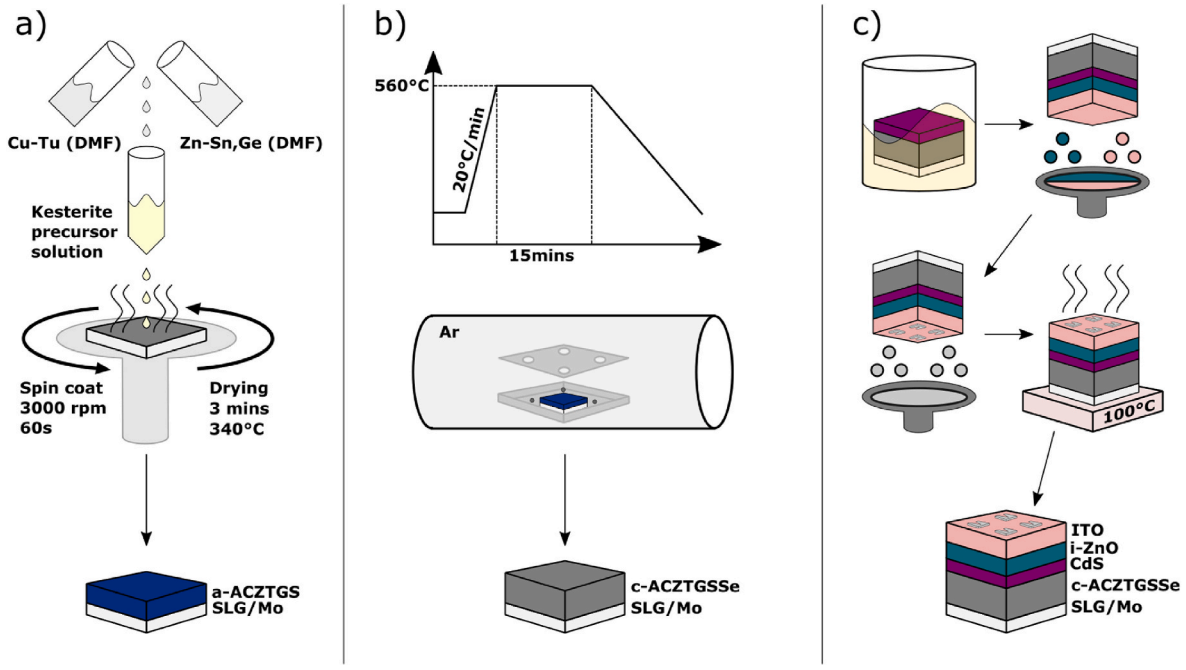

Fig. 1. Fabrication process of the ACZTGSSe thin-film solar cells. (a) Preparation of the molecular ink precursor solution and spin-coating of the amorphous a-ACZTGS precursor film with around 1–1.5 μm thickness. (b) Selenization of the precursor film to grow polycrystalline c-ACZTGSSe thin-film absorbers. (c) Deposition of the CdS buffer, i-ZnO/ITO window layers and Ag grid over the finished absorber, followed by a soft annealing of the finished device.

Supplementary data.

3. Results

First of all, the growth of kesterite polycrystalline thin films can be confirmed via XRD and Raman experiments on the completed absorbers, presented in Fig. 2 for the different targeted Ge contents. The presence of the characteristic Se-rich kesterite response is observed for both type of measurements, i.e. the two A Raman modes around 200 and 180 cm^{-1} in Fig. 2a and the (112) XRD reflection around 27° in Fig. 2b). The exact XRD peak positions are given in Table 1 along with the lattice parameters a and c. The Se-rich kesterite response is by far dominant in both the Raman spectra and the XRD diffractograms, indicating well-grown ACZTGSSe thin film absorbers are obtained following the selenization of the amorphous precursor films. It is also highlighted in Fig. S1 by the transition from the main peak at 340 cm^{-1} and 28.5° for S-pure precursor film towards the much narrower peak of Se-rich absorbers at lower Raman shift and diffraction angle. The intensity of the (112) peak is roughly 5 times and 20 times higher compared to the (220) and (312) respectively at 46° and 54° in Fig. S2a). The intensity ratios of the same XRD reflections for the $CuZnSnSe_4$ (CZTSe#26–0575) and $CuZnGeSe_4$ (CZGSe#29–0914) powder diffraction reference cards are much lower, i.e. respectively 2.5 and 5. This highlights the preferential growth of the kesterite layers studied here along the (112) direction on glass/Mo substrates.

Second, the effective integration of Ge within the kesterite lattice is demonstrated by the displacement of the A Raman mode from 201.5 to 206.9 cm^{-1} and of the (112) XRD peak from 27.28° to 27.74° from 0Ge to 100Ge, as reported in numerous other studies [44–48]. A similar shift is observed on the second A Raman mode at 180 cm^{-1} in Fig. 2a), as well as on the secondary kesterite XRD peaks in Fig. S2a) and b), further emphasizing the proper incorporation of Ge inside the kesterite crystalline system. The observed shift of the XRD reflections towards higher angle proportionally to the Ge concentration is explained by the reduced atomic radius of Ge as compared to Sn and the associated diminution of the unit cell volume [44,46], shown in Table 1. For Raman measurements, the change in bonding strength between the chalcogen species (SSe) and the group IV elements (Sn-Ge) when alloying lighter and smaller Ge atoms is responsible for the displacement of the main vibrational modes [45]. Besides that, the transition of the E-type mode at 240 cm^{-1} for 0Ge towards the B-type mode at 270 cm^{-1} for 100Ge in Fig. S2c) is also reported in the literature [45,46]. The shoulder of the main A peak appearing at 225 cm^{-1} is observed more clearly than in those other studies and is likely related to one of the characteristic modes of either CZGSe or Cu_2GeSe_3 (CGSe) [45,49]. Another observation is the lower intensity of the second A Raman mode at 180 cm^{-1} for the 0Ge reference as compared to other samples including Ge. According to another study [50], this could be interpreted as the consequence of higher Cu-Zn disorder related to Cu-Zn and Cu-Sn,Ge vibrations for 0Ge. This would indicate a higher opto-electronic quality of the Ge-containing absorbers as compared to the pure-Sn reference, also discussed below based on optical measurements.

Evaluating the shift of Raman modes and XRD peaks for 40Ge, 60Ge and 80Ge in between the pureSn and pure-Ge samples should provide estimates for Ge/(Ge + Sn). These can be compared with the XRF data in Table 2, already showing close agreement with the targeted Ge content. Yet, the positions of XRD peaks and Raman bands are also affected by the

Table 1
Position of the (112) peak and lattice parameters extracted from the XRD diffractograms for each Ge concentration.

	0Ge	40Ge	60Ge	80Ge	100Ge
(112) peak position (°)	27.277	27.387	27.458	27.548	27.739
a (Å)	5.655	5.628	5.612	5.585	5.543
(Å)	11.359	11.334	11.310	11.314	11.252
$= a^2c$ (Å^3)	362.215	358.932	356.239	352.840	345.768

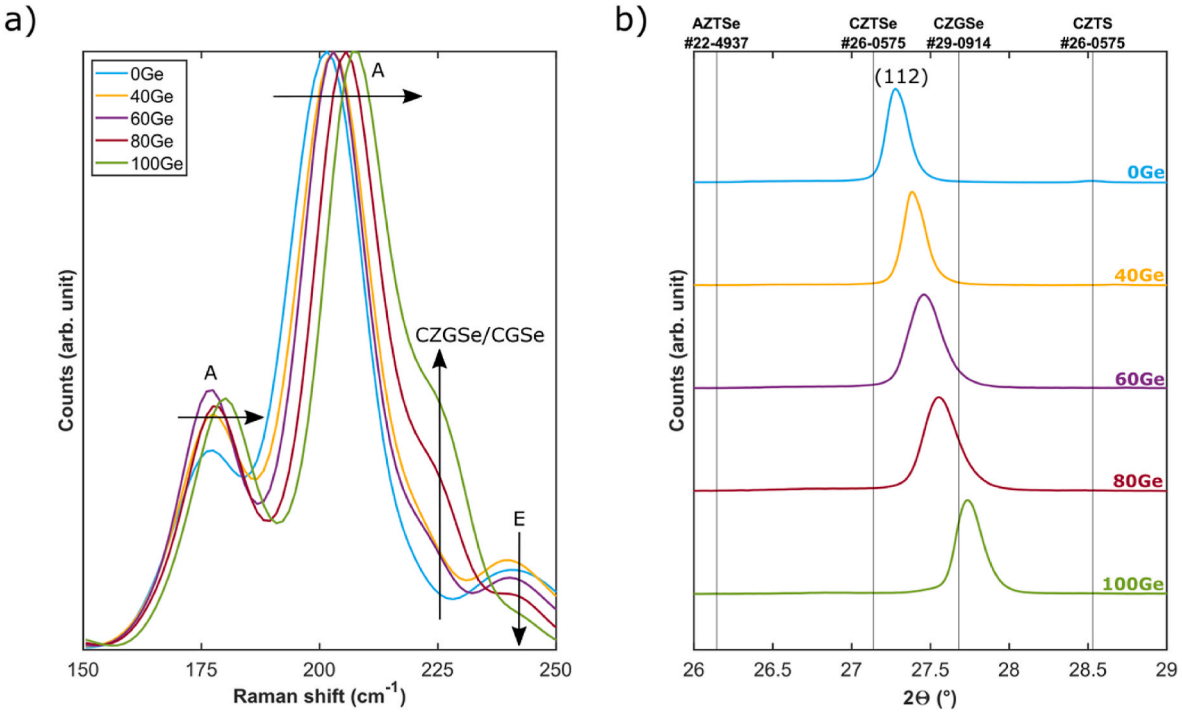

Fig. 2. Evolution of the crystalline structure of the ACZTGSSe thin-film solar cells with various Ge concentrations. (a) Normalized Raman spectra highlighting the main kesterite A modes around 180 and 200 cm^{-1}, both shifting towards higher wavenumber following the addition of Ge as shown by black arrows. The emergence of a CZGSe/Cu_2GeSe_3 contribution at 225 cm^{-1} in parallel with the E mode disappearance at 240 cm^{-1} is also emphasized. (b) XRD diffractograms showing the main kesterite (112) peak displaced towards higher angle when the Ge content is increased. The XRD Powder Diffraction reference cards of pure phase kesterites are represented to gauge the composition ranges.

Table 2
Composition ratios of ACZTGSSe kesterite absorbers estimated from XRF, Raman and XRD.

Technique	Composition ratio	0Ge	40Ge	60Ge	80Ge	100Ge
XRF	Ge/(Sn + Ge)	0	0.4	0.6	0.79	1
	Ag/(Ag + Cu)	0.15	0.13	0.15	0.14	0.15
	(Ag + Cu)/(Zn + Sn + Ge)	0.79	0.79	0.86	0.88	0.89
	Zn/(Sn + Ge)	0.99	1.06	1.04	0.99	0.98
Raman	S/(S + Se)	0.04	0.02	0.01	0.01	0.01
XRD	Ge/(Sn + Ge)	0	0.27	0.40	0.60	1

group 1 elements ratio Ag/(Ag + Cu) and chalcogen proportion S/(S + Se), which must then be determined first. Using the same molarity in AgCl and CuCl for all precursor solutions logically leads to similar Ag content around the desired 15 % in all samples. Besides that, the other composition ratios (Ag + Cu)/(Zn + Sn + Ge) and Zn/(Sn + Ge) are also confirming the intended Cu-poor and slightly Zn-rich stoichiometry. Since the Raman A mode is not shifted when alloying Ag [20], it can be used to estimate the S-Se ratio by comparison with the pure phases CZTSe and CZTS respectively located at 196 and 338 cm^{-1} [46]. The A mode position around 200 cm^{-1} indicates very low S content below 5 % as shown in Table 2. This S-poor stoichiometry could be expected from absorbers processed at high temperature in a highly saturated Se atmosphere. The Se-rich composition is further supported by the much higher intensity of the main A-Se peak at 200 cm^{-1} with regards to the secondary A-S peak around 340 cm^{-1} in Fig. S2c) [15]. Having demonstrated Se-rich stoichiometry and a nearly equal Ag content in all samples, the XRD peak shift can provide a second estimation of the Ge concentration in Table 2. The XRD shift confirms a progressive increase of the Ge content with some deviation compared to the XRF ratios, likely caused by the mismatch between multi-alloyed kesterites thin-films and pure powder diffraction references. Obtaining numerical estimations from the Raman spectra is here not relevant given the very small wavenumber difference of 10 cm^{-1} between CZTSe and CZGSe [46] compared to the measurement resolution of 1.3 cm^{-1}.

Combining Raman and XRD data usually also helps gauging the presence of mixed compounds or binary phases within the kesterite absorbers, using the full range Raman spectra and XRD diffractograms provided in Fig. S2. Firstly, the main kesterite peaks have a much higher relative intensity than other maxima within both measurements. Secondly, the developed kesterite molecular ink processing route relies on Sn^{4+}, whichis believed to ensure a growth mechanism avoiding the formation of killer binary phases [18,20]. Thirdly, expect for the potential CGSe phase, no peak is emerging or disappearing when going from pure-Sn to pureGe stoichiometry. Therefore, it is unlikely for detrimental secondary phases such as (Sn,Ge)-S,Se, Zn-S,Se or Cu_x-S,Se to be largely present in the studied absorbers. Besides that, Mo(S_x,Se_{2-x}) is quite distinctively detected by XRD in all samples at fixed diffraction angles around 32 and 56° in Fig. S2b), following its usual natural formation during the high-temperature annealing in Se excess.

Such a Mo(S_x,Se_{2-x}) interlayer can be recognized in between the ACZT(G)SSe absorber and the Mo back contact on the SEM cross section images in Fig. 3 for all Ge contents, with 1–2 times lower thickness than the absorber layer as illustrated in Fig. S3. According to Fig. 3, conformal and continuous thin-film absorbers are effectively grown with micron-size welldefined crystalline grains. There is no evidence for significant secondary phases, which aligns with the large dominance of the kesterite characteristic peaks in both Raman and XRD data for all samples. From 0Ge to 60Ge, the kesterite crystals cover most of the absorber thickness which correlates well with the nearly flat profiles of all metallic elements along the ToF-SIMS profiles in Fig. 4. However, 80Ge exhibits a much denser and thicker fine-grain sub-layer along the bottom half of the absorber thickness whereas 100Ge presents an overall smeared-out morphology, as also reported in other studies also relying on the molecular ink route [13,44,51]. These observations are in agreement with the greater variations in ToF-SIMS composition levels of 80Ge and 100Ge along their thickness than for samples with lower Ge, as emphasized by the black arrows in Fig. 4. Especially, 100Ge displays a relatively important change in the Ag and Cu profiles along its bottom half, which might be at the origin of its less defined crystalline structure. The degradation of absorber morphology for 80Ge and 100Ge could also relate to the 10 times lower solubility of $GeCl_4$ in DMF compared to $SnCl_4$ [23] and the subsequent addition of HCl to circumvent this very issue, which would require further experiments to be verified. Another hypothesis for this poorer structural quality would be an excess of the liquid phase associated to Ge-rich kesterite phases with lower melting point than those including Sn [41,52]. Contrarily to kesterite layers deposited via different routes either in vacuum [30,39,41–43] or in solution [29,40], there are here no evidence for a gradientof the Sn-Ge

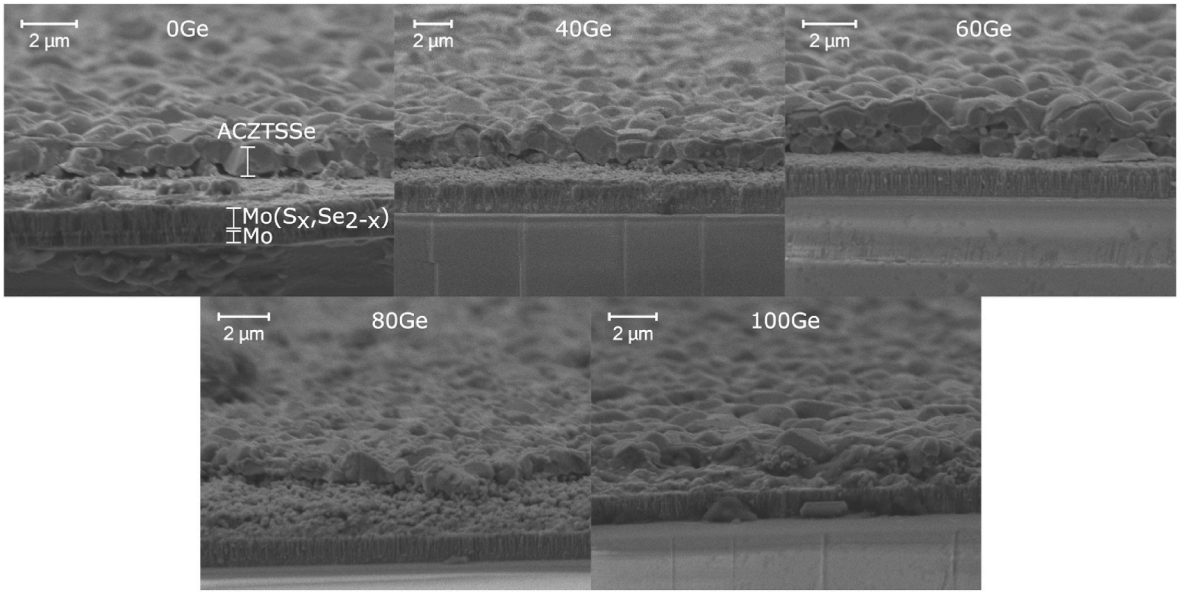

Fig. 3. Evolution of the SEM cross section of the ACZTGSSe thin-film solar cells with various Ge concentrations. The growth of polycrystalline absorbers with mostly conformal morphology is demonstrated, with a more pronounced bi-layer structure for 80Ge and 100Ge. The kesterite absorber, Mo(S_x,Se_{2-x}) interlayer and Mo back contact are shown for the Ge-free reference sample.

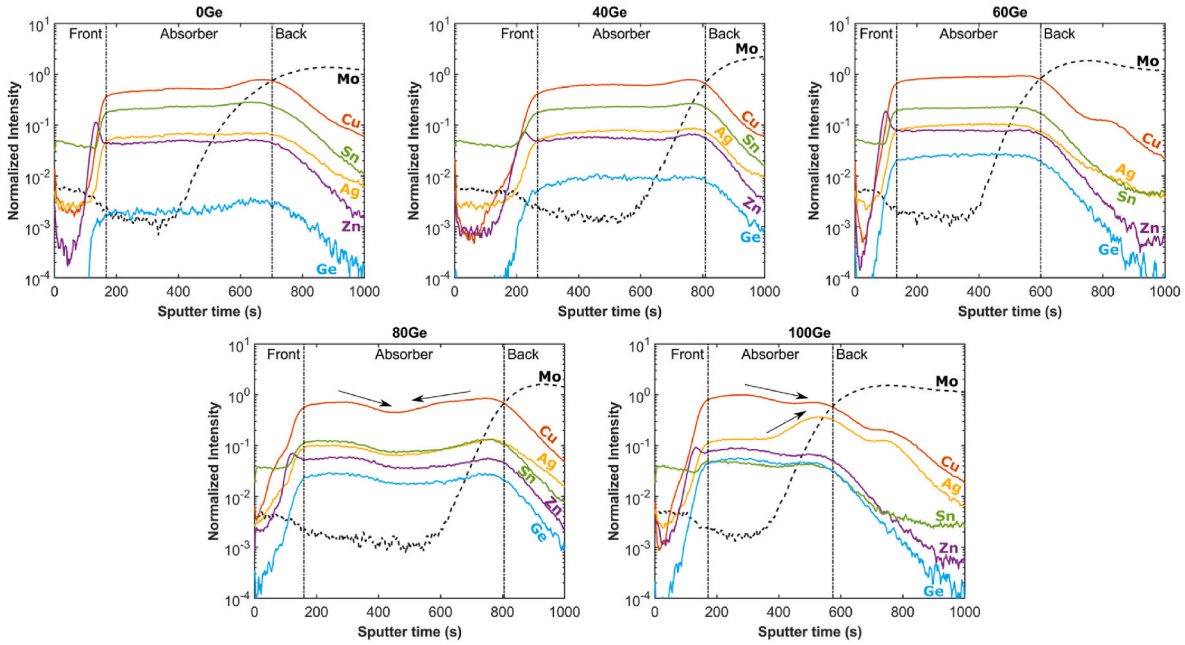

Fig. 4. Evolution of the ToF-SIMS profiles for the metallic elements of the ACZTGSSe thin-film solar cells with various Ge concentrations. The front interface with the CdS buffer and the back interface with the Mo rear electrode are shown by vertical black dotted lines, while the Mo signal is shown with a black dashed line. The black arrows highlight the variations in signal intensity and composition gradients for 80Ge and 100Ge, possibly related to their more layered morphology in Fig. 3. A specific focus on the relative thicknesses of the ACZTGSSe absorbers and the Mo(S_x,Se_{2-x}) layers along with a qualitative evolution of the Sn-Ge gradient are provided in Fig. S3.

ratio along the absorber thickness in Fig. 4. Indeed, the Sn and Ge profiles appear to always evolve in the same direction, and their ratio is mostly constant from the back to the front of the Sn-Ge mixed ACZTGSSe films (40Ge, 60Ge and 80Ge), as highlighted in Fig. S3. This can be probably explained by the solution-based processing route used here. Indeed, the formation of an amorphous kesterite precursor film with the constitutive elements already bonded to each other occurs more homogeneously than in the case of stacked precursor layers. Given the absence of Sn-Ge gradient and the negligible influence of the extremely low amount of sulfur in the absorbers, the bandgap of the studied absorbers can arguably be considered constant along their thickness.

Photoluminescence spectra of the finished devices in Fig. 5a) reveal a main peak in the expected wavelength range of the kesterites absorbers, progressively shifted to the blue for higher Ge content. The central wavelength of those peaks are considered as first estimates of the absorber bandgap, i.e. $E_{g,PL}$ shown in Table 3. The PL peak width is reduced when adding Ge, highlighting the compatibility of combined Ag- and Ge-alloying to obtain kesterite compounds with high optoelectronic quality. The clear blueshift of the EQE spectra in Fig. 5b) leads to second bandgap estimates.

$E_{g,EQE}$ in excellent agreement with $E_{g,PL}$ in Table 3. The negligible discrepancy between those two values suggests that band tailing caused

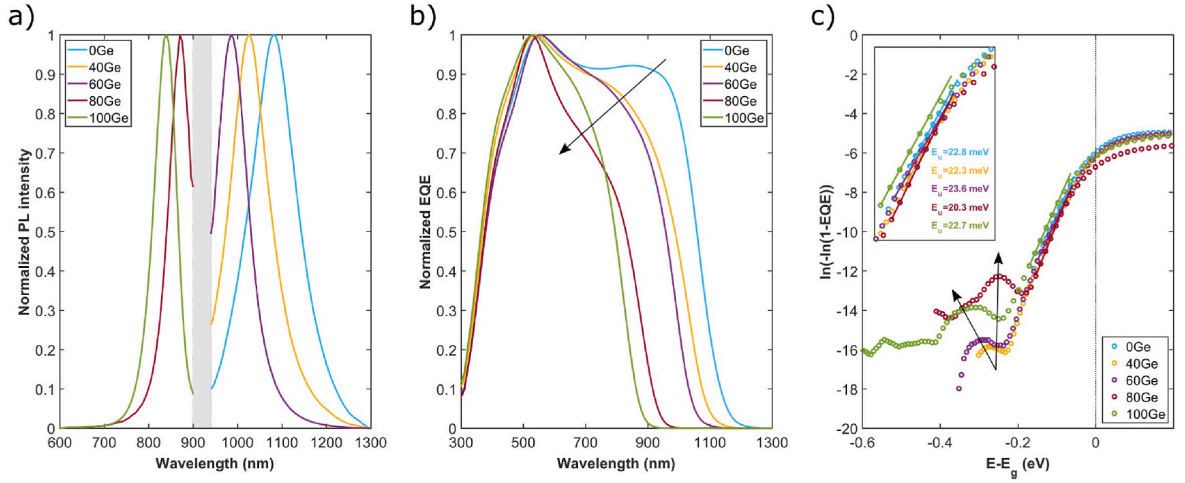

Fig. 5. (a) Normalized photoluminescence and (b) EQE spectra of the ACZTGSSe thin-film solar cells with various Ge concentrations. The PL peak position and the EQE absorber's edge are shifted towards higher energy following the bandgap increase due to higher Ge content. Despite the decrease in quantum efficiency of the low- and high-wavelength detectors in (a), shown by the gray area from 900 to 930 nm, the absorber bandgaps of the 60 and 80Ge devices can be extracted accurately from the PL peak position. (c) Extraction of the Urbach energy (E_U) for energies below the absorber bandgap. The black arrows highlight the poorer collection efficiency and the emergence of sub-bandgap contributions for 80 and 100Ge. The inset magnifies the linear extrapolation to obtain E_U and the corresponding estimates.

Table 3
Device parameters extracted from PL, EQE and 1 sun IV data for the champion device of each Ge concentration batch.

	0Ge	40Ge	60Ge	80Ge	100Ge
$E_{g,PL}$ (eV)	1.15	1.21	1.26	1.43	1.48
Eg,EQE (eV)	1.14	1.19	1.24	1.40	1.49
E_U (meV)	22.8	22.3	23.6	20.3	22.7
J_{sc} (mA/cm^2)	32.89	31.59	27.48	22.12	20.35
V_{oc} (mV)	527	592	618	650	647
FF (%)	65.93	64.89	55.78	45.06	41.21
η (%)	11.42	12.13	9.47	6.48	5.43

by crystalline disorder as well as bandgap and potential fluctuations are not significant inside the kesterite absorbers processed herein [9,53]. This aligns with the rather low Urbach energy (E_U) values between 20 and 23 meV obtained in Fig. 5c) and Table 3, which is rather expected for kesterites including Ag or low to moderate amounts of Ge [17,20,22,30,33,54]. This is turn could relate to a reduced density of the [$2I_{II}$ + IV_{II}] defect complex, due to an increased formation energy when alloying Ag and the monovalency of Ge in the 4+ oxidation state [55]. However, for the Ge-rich kesterite samples studied here with bandgaps larger than 1.2 eV, i.e. 60Ge, 80Ge and 100Ge, E_U is not increased at all. This demonstrates the ability of the proposed recipe to preserve the opto-electronic quality of Gealloyed kesterite absorbers with wider bandgaps, contrarily to previous works [36,37,54,56]. Exploring further the sub-bandgap region of the EQE spectra in Fig. 5c), emerging contributions are observed for 80Ge and 100Ge as highlighted by the black arrows. Seeing such responses for photon energies below the absorber bandgap relates to intermediate defect states, as reported in other studies for different types of PV materials [2,57]. The appearance of those peaks for the high-Ge samples correlates relatively well with literature studies also reporting changes in sub-bandgap optical transitions and dominant defects with the Ge content [35,58,59]. Eventually, the enhancement of nonradiative recombination via those bandgap states might explain the degraded EQE of the 80Ge and 100Ge devices in the absorber wavelength range, i.e. following the black arrow in Fig. 5b).

The PV parameters, i.e. V_{oc}, short-circuit current density (J_{sc}), fill factor (FF) and efficiency (η) of the champion device per Ge concentration are reported in Table 3 and obtained from the 1 sun IV curves in Fig. 6a). Given the varying absorber bandgap, computing the deficits in J_{sc}, V_{oc} and FF with respect to the Shockley-Queisser (SQ) limit ensures more straightforward comparisons. More precisely, $X_{SQdef} = X_{SQ} - X$ where $X = J_{sc}$, V_{oc} or FF and X_{SQ} are extracted from a literature report [60]. Those SQ deficits are provided in Table S1 for the champion cells and depicted along with other representative devices in Fig. 6b) for V_{oc} and in Fig. S4 for J_{sc} and FF. The gradual increase of V_{oc} from 527 to 647 mV and decrease of J_{sc} from 32.89 to 20.35 mA/cm^2 following the arrows in Fig. 6a) logically relate to the wider absorber bandgap as more Ge is incorporated. The optimal composition appears to be 40Ge with a champion efficiency of 12.1 %. The devices with Ge-richer stoichiometries exhibit lower PCEs. Indeed, 60Ge approaches the 10 % efficiency barrier while 80Ge and 100Ge suffer from rather large performance diminution down to 6.5 and 5.5 % respectively. The rather low J_{sc} deficit around 10 mA/cm^2 observed for all samples demonstrates that the proposed recipe enables to deposit well-grown kesterite absorbers with excellent absorption for any bandgap between 1.15 and 1.5 eV. This tends to exclude J_{sc} as possible culprit for poorer performance and rather points out towards V_{oc} and FF as the main performance limiting factors, as typically observed for kesterite solar cells. Indeed, Fig. 6b) shows promisingly low values of V_{oc} deficit around 350 mV from 0Ge to 60Ge, whereas it then skyrockets up to 500 mV and above 600 mV for 80Ge and 100Ge, respectively. These are possibly related to changes regarding the main electronic defects as hypothesized above from the sub-bandgap EQE spectra but also potentially from the conduction band mismatch with the CdS buffer layer for absorber bandgaps above 1.4 eV, as discussed below. A progressive increase of the FF deficit from pure-Sn to pure-Ge stoichiometry can be observed in Fig. S4, especially important again for 80Ge and 100Ge. This is likely connected to the poorer EQE response of those two devices.

To better understand the evolution of the PV figures-of-merit in function of the Ge content, the dark IV characteristics of representative devices in Fig. 7a) is examined. Indeed, analyzing such data provides an image of the junction properties and the importance of carrier recombination via the dark ideality factor n and saturation current density J_0, along with the prominence of parasitic current paths through the shunt resistance R_{sh}. These three figures-of-merit are presented in Fig. 7b) and attain more than decent values, i.e. $n \lesssim 2$, $J_0 \lesssim 10^{-7}$ A/cm^2 and $R_{sh} \gtrsim 10$ kΩ cm^2, for the 0Ge, 40Ge and 60Ge devices in line with their PCE close to or beyond 10 %. Their favourable n and J_0 correlate well with their low V_{oc} deficit while their high R_{sh} validate their conformal large-grain absorber morphology conjectured from Fig. 3. The optimal combination of parameters is showcased by the champion 40Ge device, i.e. good junction quality with $n = 1.85$ and $J_0 = 7.6*10^{-9}$ A/cm^2 as well as mostly leakage-free structure with $R_{sh} = 4.76*10^4$ Ω cm^2. Despite retaining promising values of $J_0 \simeq 10^{-7}$ A cm^2 and $R_{sh} \simeq 10^4$ Ω cm^2 that suggest preserved absorber structural quality, the performance of 80Ge is dropping significantly. This is likely the consequence of n surpassing 2

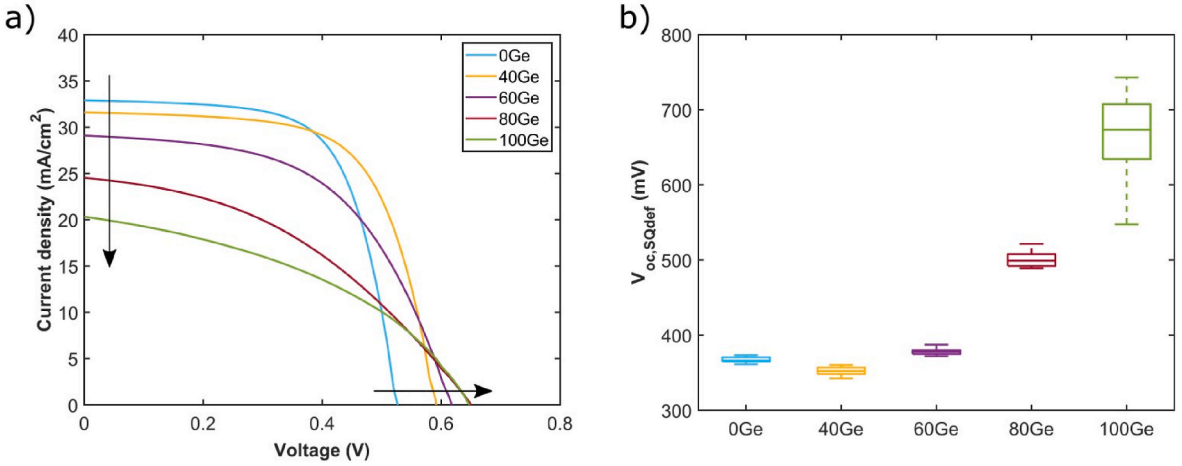

Fig. 6. (a) IV curves obtained under 1 sun illumination for the champion devices per Ge concentration. The black arrows highlight the increase and decrease of V_{oc} and J_{sc} following the bandgap increments due to higher Ge content. (b) Statistical dispersion of the V_{oc} deficit with respect to the Shockley-Queisser limit for representative devices of each Ge content, exhibiting a minimum around 340 mV for 40Ge.

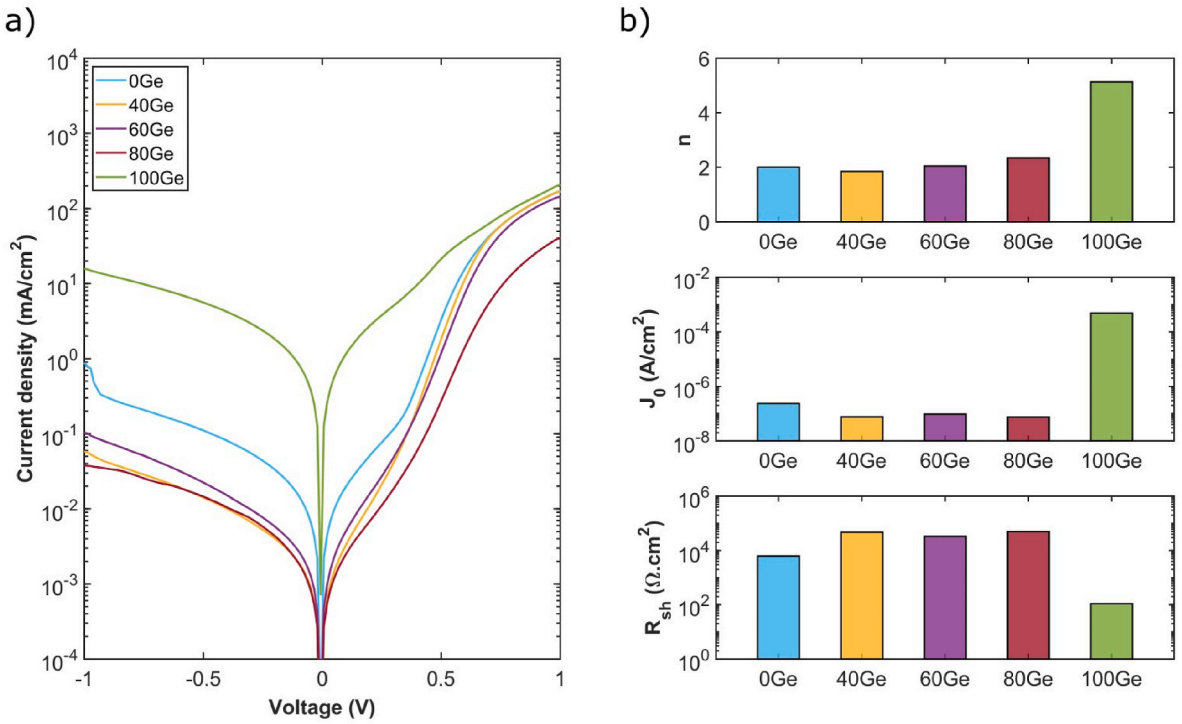

Fig. 7. (a) Dark IV curves for the ACZTGSSe devices with various Ge concentrations. (b) Corresponding parameters: ideality factor n, saturation current density J_0 and shunt resistance R_{sh}. All three figures-of-merit preserve encouraging values for 40Ge and 60Ge, R_{sh} and J_0 remain favourable whereas n is slightly degraded for 80Ge while a global degradation is observed for 100Ge.

which indicates an increase in carrier recombination and consequently losses in V_{oc}. This poorer charge extraction and collection also correlates with the degraded EQE response of 80Ge and the hypothesized emergence of sub-bandgap states, which would explain the lower FF. Alloying even more Ge induces a critical decrease of R_{sh} down to the order of 100 Ω cm^2 for 100Ge, thus clearly dominating its IV

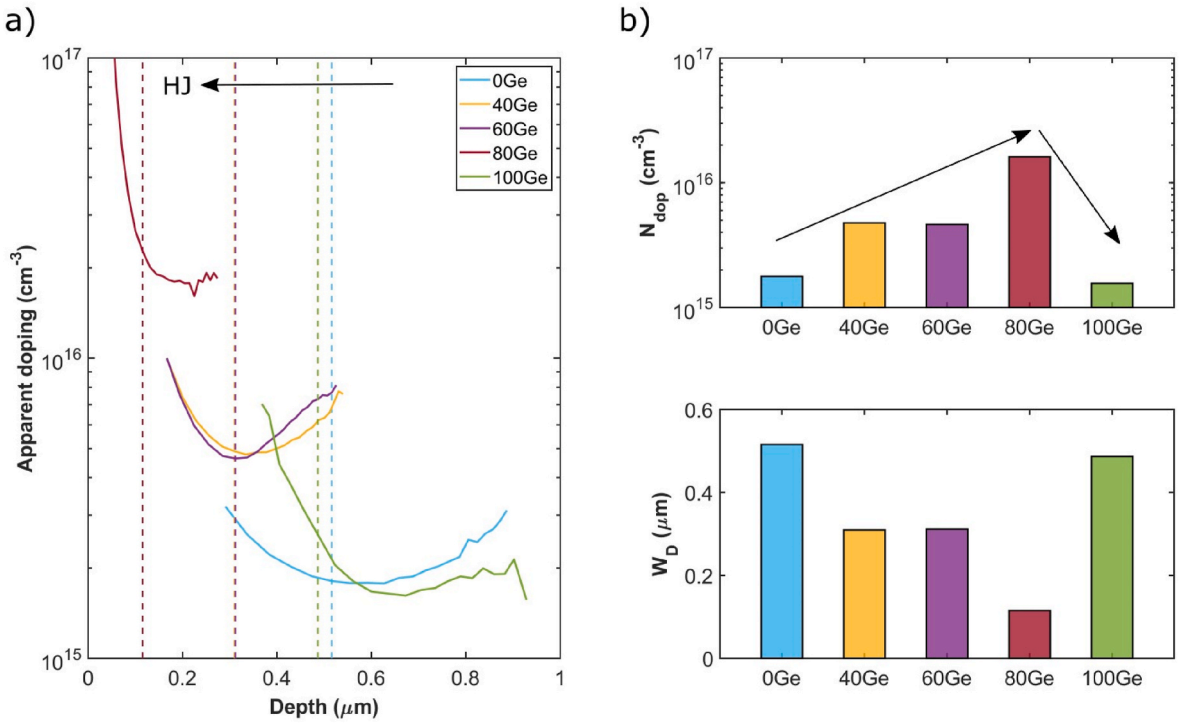

Fig. 8. (a) Apparent doping profiles for the ACZTGSSe devices with various Ge concentrations, for voltages between −0.75 V and 0.25 V and at a frequency of 10 kHz. The black arrow points towards the HJ while the vertical dashed lines indicate the data point corresponding to 0V applied bias (superimposed for 40Ge and 60Ge). (b) Evolution of the corresponding free carrier concentration N_{dop} and depletion width W_D. As highlighted by the black arrows, N_{dop} increases from 0Ge to 80Ge followed by a collapse until 100Ge. W_D follows the inverse trend compared to N_{dop} since they are inversely proportional to each other.

characteristic as compared to other devices. This leads to less ideal diode parameters n and J_0 which can largely justify the lower performance associated to greater V_{oc} and FF deficits.

To further investigate the physical origin of those efficiency barriers for 80Ge and 100Ge, capacitancevoltage-frequency (CVf) experiments are realized in the dark to provide complementary information about the device internal behaviour and limitations. Those measurements are performed with similar resolution in both frequency and voltage so as to obtain admittance spectroscopy "loss maps" shown in Fig. S5 and described in previous studies [66,67]. This representation of capacitance variations with both frequency and voltage is useful to possibly detect, identify and locate loss mechanisms affecting solar cell devices, appearing as red areas over the blue map background. On the loss maps in Fig. S5, the voltage range from −0.75 V to 0.25 V at the fixed frequency of 10 kHz offers no overlap with the possible loss mechanism signatures coloured in red, hence it was used for the apparent doping profiles displayed in Fig. 8a). This ensures that the apparent doping can be analyzed independently from other chargerelated phenomena and its value is closer to the actual free carrier concentration. This is especially important for the low-efficiency devices 80Ge and 100Ge which exhibit such signatures over large voltage-frequency domains respectively in the top right and bottom right corner of their respective loss maps. Considering this, the free carrier density N_{dop} is extracted as the minimum point of the charge profile, represented in Fig. 8b). Starting from a value of approximately $2*10^{15}$ cm^{-3} for 0Ge, N_{dop} is nearly doubled for 40Ge and 60Ge and then increases by one order of magnitude up to $2*10^{16}$ cm^{-3} for 80Ge. This increase of apparent doping from 0Ge to 80Ge content could be caused by the addition of Ge-related shallow states Cu_{Ge} and V_{Ge}, as reported elsewhere [29]. However, the enhanced N_{dop} of 80Ge does not lead to an improved device performance, for two reasons. First, its depletion width W_D is greatly reduced due to the higher doping visible in Fig. 8b), which deteriorates carrier extraction and likely explains the largely degraded EQE. Second, all the additional bandgap states induced by substituting Ge to Sn are not necessarily shallow doping levels. On the contrary, certain of those intrinsic defects may possess deep energy levels within the absorber bandgap and act as recombination centers which induce the increase of n compared to lower-Ge samples. Such traps could possibly be responsible for the large signature on the 80Ge loss map in Fig. S5 [66]. This defect-like signature appears located near the kesterite/CdS HJ interface following the white arrow direction. It matches also quite well with the steep increase of the apparent doping of 80Ge towards low depths in Fig. 8a) and correlates with the appearance of surface defects for Ge-rich kesterites studied in other works [35,58]. Eventually, for 100Ge, N_{dop} falls back to a similar level as 0Ge, which translates into a recovered W_D and probably accounts for the improved EQE as compared to 80Ge. In parallel with this evolution of the defect landscape following the Ge concentration, the band structure is changing as well since not only the absorber bandgap is becoming wider but the electronic affinity is also lowered [58,59,68]. In particular, the heterojunction conduction band alignment, which is key to determine the final device performance, transitions from a favourable spike-like barrier to an undesired cliff-like alignment at the ACZTGS-Se/CdS interface when reaching Ge-rich composi-tions. This in turn would be the main cause for the high DC current signature on the 100Ge loss map in Fig. S5, and also for the V_{oc} saturation under light for that sample [35,59].

The main outcome of this work is that adding moderate amounts of Ge to the ACTZSSe baseline recipe maintains highly promising PCEs of 12.1 % and 9.7 % for 40Ge and 60Ge respectively, with still much room for improvement regarding FF and J_{sc}. Those constitute record efficiencies for Ge-alloyed kesterite solar cells with bandgaps of 1.2 and 1.25 eV as illustrated in Fig. 9a). In particular, the optimal performance is obtained by the 40Ge champion cell showcasing a remarkably low V_{oc} deficit around 340 mV, corresponding to around 62 % of the detailed balance limit for its bandgap, which is above most other Ge-alloyed kesterite studies. For this device, the quasi absence of low-temperature

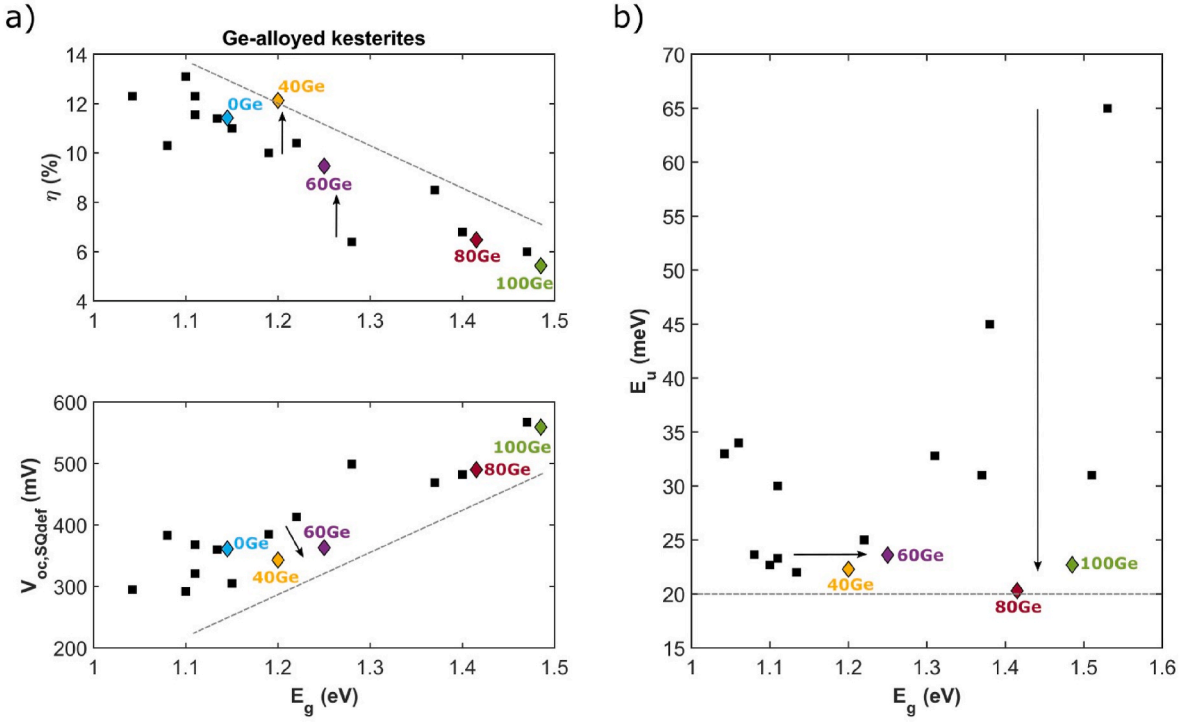

Fig. 9. (a) Representation of the obtained champion efficiencies and corresponding V_{oc} SQ deficits with respect to the absorber bandgap (coloured diamonds), compared to other values reported in literature for Ge-alloyed kesterites (black squares) [22,23,29,30,32,33,36,37,54,61–63]. The black arrows emphasize the higher efficiency and lower V_{oc} deficit for devices with bandgaps between 1.2 and 1.25 eV. (b) Urbach energy E_U of the champion devices presented in this study (coloured diamonds), in comparison with other studies about all types of kesterites (black squares) [12,22,27,29,30,32,33,36,37,54,64,65]. The black arrows highlight the maintained low E_U values around 20 meV for all bandgaps between 1.15 and 1.5 eV. The gray dashed lines are guides to the eye.

rollover for V_{oc} in Fig. S6 indicates negligible second order effects and thus reliable linear extrapolation until 0K [68]. The resulting V_{oc} at 0 K only has a 50 mV discrepancy with the 1.2 eV bandgap which constitutes evidence for a high-performance potential. These record V_{oc} deficits can surely be attributed to some extent to the low E_U values around 20 meV obtained for all samples [69]. As illustrated in Fig. 9b), this study is one the very few showing such a preservation of the small Urbach tail while increasing the bandgap of a kesterite absorber of any type. This sets an excellent baseline in terms of material opto-electronic quality before proceeding to further device performance optimization for the high-Ge samples. Indeed, the record V_{oc} deficits observed for the 80Ge and 100Ge devices do not translate into record efficiencies. This could originate from the various mechanisms mentioned above, namely variations of the defect states coupled to conduction band misalignment and less efficient carrier extraction, all inducing V_{oc} and FF losses. Potential solutions could for instance include a more adapted buffer material for absorber bandgaps above 1.4 eV [63], an alternative to HCl for reaching complete dissolution of the Ge precursors or heterojunction interface passivation [36]. Those should be combined with a deeper understanding of the interaction between defect landscape and band structure, and its evolution for higher Ge concentration, which are some of the numerous possible follow-up studies to this work.

4. Conclusions

To conclude, this work implements a molecular ink chemical route for processing high-quality Ag,Gealloyed kesterite absorbers with great device performance potential in a wide range of bandgaps. During the simple preparation of the precursor solution and film in ambient air, the ratio of Sn and Ge salts is varied to cover the whole Ge composition spectrum from 0 to 100 %. Ge contents beyond 40 % are especially investigated, demonstrating the potential of the presented recipe to complement the existing literature mostly limited to lower Ge concentrations. The ACZTGSSe thin films obtained after selenization exhibit excellent polycrystalline morphology, no secondary phases nor structural flaws. These absorbers properly integrate Ge into their lattice, which allows flexible tuning of their bandgap from 1.15 to 1.5 eV when ranging from pureSn to pure-Ge stoichiometry. The champion efficiency of 12.1 % obtained for 40 % Ge without ARC sets a new record for Ge-alloyed kesterites solar cells with a bandgap of 1.2 eV. This is mainly the consequence of an outstanding 62 % of the V_{oc} Shockley-Queisser limit reached for this device, with still room for improvement regarding J_{sc} and FF. The developed process interestingly maintains such encouraging PCE and V_{oc} deficit when reaching a bandgap of 1.25 eV and 60 % Ge. The reason for this promising performance 40Ge and 60Ge is two-fold. On the one hand, excellent heterojunction properties are characterized by low recombination and efficient carrier collection. On the other hand, high opto-electronic quality of the kesterite material confirmed by the low Urbach energy slightly above 20 meV. This is the very sign of mitigated crystalline disorder and benign band tailing, known to be one of the main challenges faced by kesterites. The small Urbach front is remarkably extended up to the highest bandgap of 1.5 eV for the pure-Ge sample, probably enabled by the combined alloying of Ag and Ge in solution. Therefore, the proposed deposition strategy provides an interesting solution to overcome the intrinsic limitations of kesterites in a wide range of bandgaps while proving the interest to transition from physical processes to chemical routes. This study establishes a basis for highquality kesterite materials with tunable bandgap, still.

requiring optimization regarding the evolution of defect landscape and band structure for Ge contents higher than 60 %. Tackling this latter issue may bring kesterite solar cells to a stronger position in the thin-film PV field, especially regarding tandem and indoor applications.

CRediT authorship contribution statement

Romain Scaffidi: Writing – review & editing, Writing – original draft, Visualization, Validation, Methodology, Investigation, Formal analysis, Data curation, Conceptualization. **Yuancai Gong:** Writing – review & editing, Resources, Methodology, Investigation, Formal analysis, Conceptualization. **Alex Jimenez-Arguijo:** Writing – review & editing, Resources, Methodology, Investigation, Formal analysis, Conceptualization. **Axel Gon Medaille:** Investigation, Formal analysis. **Sunil Suresh:** Writing – review & editing. **Guy Brammertz:** Writing – review & editing, Supervision, Project administration, Funding acquisition. **Sergio Giraldo:** Writing – review & editing. **Joaquim Puigdollers:** Writing – review & editing. **Denis Flandre:** Writing – review & editing, Supervision. **Bart Vermang:** Writing – review & editing, Supervision, Project administration, Funding acquisition. **Edgardo Saucedo:** Writing – review & editing, Supervision, Resources, Project administration, Funding acquisition.

Declaration of competing interest

The authors declare that they have no known competing financial interests or personal relationships that could have appeared to influence the work reported in this paper.

Acknowledgements

This project received funding from the European Union's H2020 research and innovation programme under grant agreement number 952982 (CUSTOM-ART). R.S. thanks FWO for the funding through the Fundamental Research PhD Fellowship (1178024N) and Travel Grant for a long stay abroad (V462623N). Y.G. thanks the European Union's Horizon 2020 research and innovation programme under the Marie Skłodowska-Curie grant agreement No 10115148. A.J.A. acknowledges the funding from Agencia Estatal de Investigacion, MICINN Spain, project ACT-FAST (PCI2023-145971-2) from the CETP-Partnership Program 2022. S.G. thanks the Juan de la Cierva grant IJC2020-044716-I funded by MCIN/AEI/10.13039/501100011033 and by the European Union NextGenerationEU/PRTR. E.S. is grateful to ICREA Academia program.

Appendix A. Supplementary data

Supplementary data to this article can be found online at https://doi.org/10.1016/j.mtener.2024.101715.

Data availability

Data will be made available on request.

References

[1] B. Vermang, G. Brammertz, M. Meuris, T. Schnabel, E. Ahlswede, L. Choubrac, S. Harel, C. Cardinaud, L. Arzel, N. Barreau, J. Van Deelen, P.-J. Bolt, P. Bras, Y. Ren, E. Jaremalm, S. Khelifi, S. Yang, J. Lauwaert, M. Batuk, J. Hadermann, X. Kozina, E. Handick, C. Hartmann, D. Gerlach, A. Matsuda, S. Ueda, T. Chikyow, R. Felix, Y. Zhang, R.G. Wilks, M. Bär, Wide band gap kesterite absorbers for thin film solar cells: potential and challenges for their deployment in tandem devices, Sustain. Energy Fuels 3 (2019) 2246–2259, https://doi.org/10.1039/C9SE00266A.

[2] D. Wang, H. Guo, X. Wu, X. Deng, F. Li, Z. Li, F. Lin, Z. Zhu, Y. Zhang, B. Xu, A. K. Jen, Interfacial engineering of WideBandgap perovskites for efficient perovskite/CZTSSe tandem solar cells, Adv. Funct. Mater 32 (2022) 2107359, https://doi.org/10.1002/adfm.202107359.

[3] S. Giraldo, Z. Jehl, M. Placidi, V. Izquierdo-Roca, A. Perez-ˊ Rodrıguez, E. Saucedo, Progress and perspectives of thin film kesterite photovoltaic technology: a critical review, Adv. Mater 31 (2019) 1806692, https://doi.org/10.1002/adma.201806692.

[4] R. Scaffidi, G. Birant, G. Brammertz, J. De Wild, D. Flandre, B. Vermang, Ge-alloyed kesterite thin-film solar cells: previous investigations and current status – a comprehensive review, J. Mater. Chem. A 11 (2023) 13174–13194, https://doi.org/10.1039/D3TA01218B.

[5] S. Khelifi, G. Brammertz, L. Choubrac, M. Batuk, S. Yang, M. Meuris, N. Barreau, J. Hadermann, H. Vrielinck, D. Poelman, K. Neyts, B. Vermang, J. Lauwaert, The path towards efficient wide band gap thin-film kesterite solar cells with transparent back contact for viable tandem application, Sol. Energy Mater. Sol. Cell 219 (2021) 110824, https://doi.org/10.1016/j.solmat.2020.110824.

[6] T. Todorov, T. Gershon, O. Gunawan, C. Sturdevant, S. Guha, Perovskite-kesterite monolithic tandem solar cells with high open-circuit voltage, Appl. Phys. Lett 105 (2014) 173902, https://doi.org/10.1063/1.4899275.

[7] K. Sun, F. Liu, X. Hao, Kesterite Cu $_2$ ZnSnS $_{4-x}$ Se $_x$ thin film solar cells, in: B. Zaidi, C. Shekhar (Eds.), Thin Films Photovoltaics, IntechOpen, 2022. https://www.intechopen.com/chapters/79871, 10. 5772/intechopen.101744.

[8] M. He, C. Yan, J. Li, M.P. Suryawanshi, J. Kim, M.A. Green, X. Hao, Kesterite solar cells: insights into current strategies and challenges, Adv. Sci 8 (2021) 2004313, https://doi.org/10.1002/advs.202004313.

[9] T. Gokmen, O. Gunawan, T.K. Todorov, D.B. Mitzi, Band tailing and efficiency limitation in kesterite solar cells, Appl. Phys. Lett 103 (2013) 103506, https://doi.org/10.1063/1.4820250.

[10] J. Li, J. Huang, F. Ma, H. Sun, J. Cong, K. Privat, R.F. Webster, S. Cheong, Y. Yao, R. L. Chin, X. Yuan, M. He, K. Sun, H. Li, Y. Mai, Z. Hameiri, N.J. Ekins-Daukes, R. D. Tilley, T. Unold, M.A. Green, X. Hao, Unveiling microscopic carrier loss mechanisms in 12% efficient Cu2ZnSnSe4 solar cells, Nat. Energy 7 (2022) 754–764, https://doi.org/10.1038/s41560-022-01078-7.

[11] T. Gershon, D. Bishop, P. Antunez, S. Singh, K.W. Brew, Y.S. Lee, O. Gunawan, T. Gokmen, T. Todorov, R. Haight, Unconventional kesterites: the quest to reduce band tailing in CZTSSe, Curr. Opin. Green Sustainable Chem 4 (2017) 29–36, https://doi.org/10.1016/j.cogsc.2017.01.003.

[12] D.W. Miller, C.W. Warren, O. Gunawan, T. Gokmen, D.B. Mitzi, J.D. Cohen, Electronically active defects in the Cu2ZnSn(Se,S)4 alloys as revealed by transient photocapacitance spectroscopy, Appl. Phys. Lett 101 (2012) 142106, https://doi.org/10.1063/1.4754834.

[13] T. Schnabel, M. Seboui, E. Ahlswede, Band gap tuning of Cu2ZnGeSxSe4-x absorbers for thin-film solar cells, Energies 10 (2017) 1813, https://doi.org/10.3390/en10111813.

[14] J. Andrade-Arvizu, V. Izquierdo-Roca, I. Becerril-Romero, P. Vidal-Fuentes, R. Fonoll-Rubio, Y. Sanchez, M. Placidi, L. Calvo-Barrio, O. Vigil-Galan, E. Saucedo, Is it possible To' develop complex S–Se graded band gap profiles in KesteriteBased solar cells? ACS Appl. Mater. Interfaces 11 (2019) 32945–32956, https://doi.org/10.1021/acsami.9b09813.

[15] F. Liu, F. Zeng, N. Song, L. Jiang, Z. Han, Z. Su, C. Yan, X. Wen, X. Hao, Y. Liu, Kesterite Cu $_2$ ZnSn(S,Se) $_4$ solar cells with beyond 8% efficiency by a sol–gel and selenization process, ACS Appl. Mater. Interfaces 7 (2015) 14376–14383, https://doi.org/10.1021/acsami.5b01151.

[16] M.A. Green, E.D. Dunlop, M. Yoshita, N. Kopidakis, K. Bothe, G. Siefer, X. Hao, Solar cell efficiency tables (Version 63), Progress in Photovoltaics 32 (2024) 3–13, https://doi.org/10.1002/pip.3750.

[17] Y. Gong, A. Jimenez-Arguijo, A.G. Medaille, S. Moser, A. Basak, R. Scaffidi, R. Carron, D. Flandre, B. Vermang, S. Giraldo, H. Xin, A. Perez-Rodriguez, E. Saucedo, Li-doping and Ag-alloying interplay shows the pathway for kesterite solar cells with efficiency over 14, Adv. Funct. Mater (2024) 2404669, https://doi.org/10.1002/adfm.202404669.

[18] J. Zhou, X. Xu, H. Wu, J. Wang, L. Lou, K. Yin, Y. Gong, J. Shi, Y. Luo, D. Li, H. Xin, Q. Meng, Control of the phase evolution of kesterite by tuning of the selenium partial pressure for solar cells with 13.8% certified efficiency, Nat. Energy 8 (2023) 526–535, https://doi.org/10.1038/s41560-023-01251-6.

[19] J. Shi, J. Wang, F. Meng, J. Zhou, X. Xu, K. Yin, L. Lou, M. Jiao, B. Zhang, H. Wu, Y. Luo, D. Li, Q. Meng, Multinary alloying for facilitated cation exchange and suppressed defect formation in kesterite solar cells with above 14% certified efficiency, Nat. Energy (2024), https://doi.org/10.1038/s41560-024-01551-5.

[20] Y. Gong, R. Qiu, C. Niu, J. Fu, E. Jedlicka, R. Giridharagopal, Q. Zhu, Y. Zhou, W. Yan, S. Yu, J. Jiang, S. Wu, D.S. Gin- ger, W. Huang, H. Xin, Ag incorporation with controlled grain growth enables 12.5% efficient kesterite solar cell with open circuit voltage reached 64.2% shockley–queisser limit, Adv. Funct. Mater 31 (2021) 2101927, https://doi.org/10.1002/adfm.202101927.

[21] Y. Cui, M. Wang, P. Dong, S. Zhang, J. Fu, L. Fan, C. Zhao, S. Wu, Z. Zheng, DMF-based large-grain spanning Cu $_2$ ZnSn(S $_x$,Se $_{1-x}$) $_4$ device with a PCE of 11.76, Adv. Sci 9 (2022) 2201241, https://doi.org/10.1002/advs.202201241.

[22] J. Wang, J. Zhou, X. Xu, F. Meng, C. Xiang, L. Lou, K. Yin, B. Duan, H. Wu, J. Shi, Y. Luo, D. Li, H. Xin, Q. Meng, Ge bidirectional diffusion to simultaneously engineer back interface and bulk defects in the absorber for efficient CZTSSe solar cells, Adv. Mater 34 (2022) 2202858, https://doi.org/10.1002/adma.202202858.

[23] J.A. Clark, A. Murray, J.-m. Lee, T.S. Autrey, A.D. Collord, H.W. Hillhouse, Complexation chemistry in *N,N* dimethylformamide-based molecular inks for chalcogenide semiconductors and photovoltaic devices, J. Am. Chem. Soc 141 (2019) 298–308, https://doi.org/10.1021/jacs.8b09966.

[24] Y.E. Romanyuk, S.G. Haass, S. Giraldo, M. Placidi, D. Tiwari, D.J. Fermin, X. Hao, H. Xin, T. Schnabel, M. Kauk-Kuusik, P. Pistor, S. Lie, L.H. Wong, Doping and alloying of kesterites, J. Phys. Energy 1 (2019) 044004, https://doi.org/10.1088/2515-7655/ab23bc.

[25] Q. Tian, S.F. Liu, Defect suppression in multinary chalcogenide photovoltaic materials derived from kesterite: progress and outlook, J. Mater. Chem. A 8 (2020) 24920–24942, https://doi.org/10.1039/D0TA08202C.

[26] S. Moser, A. Aribia, R. Scaffidi, E. Gilshtein, G. Brammertz, B. Vermang, A. N. Tiwari, R. Carron, Controlled Li alloying by postsynthesis electrochemical treatment of Cu $_2$ ZnSn(S, Se) $_4$ absorbers for solar cells, ACS Appl. Energy Mater 6 (2023) 12515–12525, https://doi.org/10.1021/acsaem.3c02483.

[27] C. Yan, K. Sun, J. Huang, S. Johnston, F. Liu, B.P. Veettil, K. Sun, A. Pu, F. Zhou, J. A. Stride, M.A. Green, X. Hao, Beyond 11% efficient sulfide kesterite Cu $_2$ Zn $_x$ Cd $_{1-x}$ SnS 4 solar cell: effects of cadmium alloying, ACS Energy Lett 2 (2017) 930–936, https://doi.org/10.1021/acsenergylett.7b00129.

[28] Z. Su, J.M.R. Tan, X. Li, X. Zeng, S.K. Batabyal, L.H. Wong, Cation substitution of solution-processed Cu $_2$ ZnSnS $_4$ thin film solar cell with over 9% efficiency, Adv. Energy Mater 5 (2015) 1500682, https://doi.org/10.1002/aenm.201500682.

[29] J. Fu, D. Kou, W. Zhou, Z. Zhou, S. Yuan, Y. Qi, S. Wu, Ag, Ge dual-gradient substitution for low-energy loss and highefficiency kesterite solar cells, J. Mater. Chem. A 8 (2020) 22292–22301, https://doi.org/10.1039/D0TA06318E.

[30] J. Liu, Z. Liu, K. Gao, H. Cai, Y. Liu, W. Zhao, X. Liu, K. Cheng, Z. Du, Back shallow Ge gradient enhanced carrier separation for CZTSe solar cells through a coselenization process, ACS Appl. Mater. Interfaces 13 (2021) 56302–56308, https://doi.org/10.1021/acsami.1c16861.

[31] Y. Atasoy, E. Bacaksız, A. Çiriş, M.A. Olgar, R. Zan, A.M. Al-dala Ali, T. Küçükömeroğlu, B.M. Başol, Improved CZTSẽ solar cell efficiency via silver and germanium alloying, Sol. Energy 267 (2024) 112247, https://doi.org/10.1016/j.solener.2023.112247.

[32] M.C. Baek, J.S. Jang, V.C. Karade, M.P. Suryawanshi, J. Kim, T.E. Hong, S.W. Park, S.W. Shin, J.H. Kim, Achieving highly efficient kesterite solar cells using simultaneous surface Ge substitution and rear interface engineering strategies, Chem. Eng. J 479 (2024) 147842, https://doi.org/10.1016/j.cej.2023.147842.

[33] X. Tan, J. Hu, W. Zhu, F. Wu, X. Han, Improved performance of kesterite Cu2ZnSn(S,Se)4 thin film solar cells by Ag/Ge codoping 981 (2024) 173645, https://doi.org/10.1016/j.jallcom.2024.173645.

[34] C. Xu, Q. Li, Q. Song, Y. Zhao, X. Hu, Z. Zhou, Y. Zhang, Y. Chen, X. Su, L. Wu, S. Wang, Analyzing the synergistic effect of Ag and Ge co-incorporation on Cu2ZnSnSe4 thin-film solar cells, Mater. Today Energy 40 (2024) 101518, https://doi.org/10.1016/j.mtener.2024.101518.

[35] A.D. Collord, H.W. Hillhouse, Germanium alloyed kesterite solar cells with low voltage deficits, Chem. Mater 28 (2016) 2067–2073, https://doi.org/10.1021/acs.chemmater.5b04806.

[36] L. Choubrac, M. Bar, X. Kozina, R. Felix, R.G. Wilks, G. Bram-′ mertz, S. Levcenko, L. Arzel, N. Barreau, S. Harel, M. Meuris, B. Vermang, Sn substitution by Ge: strategies to overcome the open-circuit voltage deficit of kesterite solar cells, ACS Appl. Energy Mater 3 (2020) 5830–5839, https://doi.org/10.1021/acsaem.0c00763.

[37] D. Nowak, T. Khonsor, D. Pareek, L. Gütay, Vapor-phase In-corporation of Ge in CZTSe absorbers for improved stability of high-efficiency kesterite solar cells, Appl. Sci 12 (2022) 1376, https://doi.org/10.3390/app12031376.

[38] C.J. Hages, S. Levcenco, C.K. Miskin, J.H. Alsmeier, D. Abou-Ras, R.G. Wilks, M. Bar, T. Unold, R. Agrawal, Im-proved performance of Ge-alloyed CZTGeSSe thin-film solar cells through control of elemental losses, Progress in Photovoltaics 23 (2015) 376–384, https://doi.org/10.1002/pip.2442.

[39] R. Scaffidi, G. Brammertz, Y. Wang, A.U. Zaman, K. Sasikumar, J. De Wild, D. Flandre, B. Vermang, A study of bandgapgraded CZTGSe kesterite thin films for solar cell applications, Energy Adv 2 (2023) 1626–1633, https://doi.org/10.1039/D3YA00359K.

[40] I. Kim, K. Kim, Y. Oh, K. Woo, G. Cao, S. Jeong, J. Moon, Bandgap-graded Cu $_2$ Zn (Sn $_{1-x}$ Ge $_x$)S $_4$ thin-film solar cells derived from metal chalcogenide complex ligand capped nanocrystals, Chem. Mater 26 (2014) 3957–3965, https://doi.org/10.1021/cm501568d.

[41] J. Marquez, H. Stange, C.J. Hages, N. Schaefer, S. Lev-′ cenko, S. Giraldo, E. Saucedo, K. Schwarzburg, D. AbouRas, A. Redinger, M. Klaus, C. Genzel, T. Unold, R. Mainz, Chemistry and dynamics of Ge in kesterite: toward BandGap-graded absorbers, Chem. Mater 29 (2017) 9399–9406, https://doi.org/10.1021/acs.chemmater.7b03416.

[42] C. Andres, A. Cabas-Vidani, A. Tiwari, Y. Romanyuk, From sputtered metal precursors towards Cu2Zn(Sn1-x,Gex)Se4 thin film solar cells with shallow back grading, Thin. Solid. Films 665 (2018) 168–172, https://doi.org/10.1016/j.tsf.2018.09.022.

[43] J. Andrade-Arvizu, R. Fonoll-Rubio, Y. Sanchez, I. Becerril-′ Romero, C. Malerba, M. Valentini, L. Calvo-Barrio, V. Izquierdo-Roca, M. Placidi, O. Vigil-Galan, A. P.′ erez-′ Rodr′ıguez, E. Saucedo, Z. Jehl Li-Kao, Rear band gap grading strategies on Sn–Ge-alloyed kesterite solar cells, ACS Appl. Energy Mater 3 (2020) 10362–10375, https://doi.org/10.1021/acsaem.0c01146.

[44] D.B. Khadka, J. Kim, Study of structural and optical properties of kesterite Cu2ZnGeX4 (X = S, Se) thin films synthesized by chemical spray pyrolysis, CrystEngComm 15 (2013) 10500, https://doi.org/10.1039/c3ce41387j.

[45] D.B. Khadka, J. Kim, Band gap engineering of alloyed Cu $_2$ ZnGe $_x$ Sn $_{1-x}$ Q $_4$ (Q = S,Se) films for solar cell, J. Phys. Chem. C 119 (2015) 1706–1713, https://doi.org/10.1021/jp510877g.

[46] E. Garcia-Llamas, M. Guc, I. Bodnar, X. Fontane, R. Caballero, J. Merino, M. Leon, V. Izquierdo-Roca, Multiwavelength exci-′ tation Raman scattering of Cu2ZnSn1-xGex(S,Se)4 single crystals for earth abundant photovoltaic applications, J. Alloys Compd 692 (2017) 249–256, https://doi.org/10.1016/j.jallcom.2016.09.035.

[47] M. Guc, S. Levcenko, V. Izquierdo-Roca, X. Fontane, E. Arushanov, A. Perez-Rodr′ ′ıguez, Polarized Raman scattering analysis of Cu2ZnSnSe4 and Cu2ZnGeSe4 single crystals, J. Appl. Phys 114 (2013) 193514, https://doi.org/10.1063/1.4830028.

[48] R. Caballero, J. Cano-Torres, E. Garcia-Llamas, X. Fontane, A. Perez-Rodr′ ′ıguez, D. Greiner, C. Kaufmann, J. Merino, I. Victorov, G. Baraldi, M. Valakh, I. Bodnar, V. Izquierdo-Roca, M. Leon, Towards the growth of Cu 2 ZnSn 1-x Ge x S 4 thin' films by a single-stage process: effect of substrate temperature. and composition, Sol. Energy Mater. Sol. Cell 139 (2015) 1–9, https://doi.org/10.1016/j.solmat.2015.03.004.

[49] G. Marcano, C. Rincon, G. Mar′ ′ın, G. Delgado, A. Mora, J. Herrera-Perez, J. Mendoza-Alvarez, P. Rodr′ ′iguez, Raman scattering and X-ray diffraction study in Cu2GeSe3, Solid State Commun 146 (2008) 65–68, https://doi.org/10.1016/j.ssc.2008.01.018.

[50] M. Dimitrievska, A. Fairbrother, E. Saucedo, A. Perez-′ Rodr′iguez, V. Izquierdo-Roca, Influence of compositionally induced defects on the vibrational properties of device grade Cu2ZnSnSe4 absorbers for kesterite based solar cells, Appl. Phys. Lett 106 (2015) 073903, https://doi.org/10.1063/1.4913262.

[51] T. Schnabel, M. Seboui, E. Ahlswede, Evaluation of different metal salt solutions for the preparation of solar cells with widegap Cu $_2$ ZnGeS $_x$ Se $_{4-x}$ absorbers, RSC Adv 7 (2017) 26–30, https://doi.org/10.1039/C6RA23068G.

[52] S. Giraldo, E. Saucedo, M. Neuschitzer, F. Oliva, M. Placidi, X. Alcobe, V. Izquierdo-Roca, S. Kim, H. Tampo, H. Shibata, A. Perez-Rodr′ ′iguez, P. Pistor, How small amounts of Ge modify the formation pathways and crystallization of kesterites, Energy Environ. Sci 11 (2018) 582–593, https://doi.org/10.1039/C7EE02318A.

[53] S. Siebentritt, G. Rey, A. Finger, D. Regesch, J. Sendler, T.P. Weiss, T. Bertram, What is the bandgap of kesterite? Sol. Energy Mater. Sol. Cell 158 (2016) 126–129, https://doi.org/10.1016/j.solmat.2015.10.017.

[54] S. Kim, K.M. Kim, H. Tampo, H. Shibata, S. Niki, Improvement of voltage deficit of Ge-incorporated kesterite solar cell with 12.3% conversion efficiency, APEX 9 (2016) 102301, https://doi.org/10.7567/APEX.9.102301.

[55] A. Crovetto, S. Kim, M. Fischer, N. Stenger, A. Walsh, I. Chorkendorff, P.C. K. Vesborg, Assessing the defect tolerance of kesterite-inspired solar absorbers, Energy Environ. Sci 13 (2020) 3489–3503, https://doi.org/10.1039/D0EE02177F.

[56] K. Nagaya, S. Fujimoto, H. Tampo, S. Kim, M. Nishiwaki, Y. Nishigaki, M. Kato, H. Shibata, H. Fujiwara, Very small tail state formation in Cu2ZnGeSe4, Appl. Phys. Lett 113 (2018) 093901, https://doi.org/10.1063/1.5031799.

[57] C.M. Sutter-Fella, D.W. Miller, Q.P. Ngo, E.T. Roe, F.M. Toma, I.D. Sharp, M. C. Lonergan, A. Javey, Band tailing and deep defect states in CH $_3$ NH $_3$ Pb(I $_{1-x}$ Br $_x$) $_3$ perovskites as revealed by sub-bandgap photocurrent, ACS Energy Lett 2 (2017) 709–715, https://doi.org/10.1021/acsenergylett.6b00727.

[58] T. Nagai, T. Shimamura, K. Tanigawa, Y. Iwamoto, H. Hamada, N. Ohta, S. Kim, H. Tampo, H. Shibata, K. Matsubara, S. Niki, N. Terada, Band alignment of the CdS/Cu $_2$ Zn(Sn $_{1-x}$ Ge x)Se $_4$ heterointerface and electronic properties at the Cu $_2$ Zn(Sn $_{1-x}$ Ge $_x$)Se $_4$ surface: $x = 0$, 0.2, and 0.4, ACS Appl. Mater. Interfaces 11 (2019) 4637–4648, https://doi.org/10.1021/acsami.8b19200.

[59] T. Nagai, S. Kim, H. Tampo, K. Tanigawa, Y. Iwamoto, H. Hamada, N. Ohta, H. Shibata, S. Niki, N. Terada, Characterization of surface and heterointerface of Cu $_2$ ZnSn $_{1-x}$ Ge $_x$ Se $_4$ for solar cell applications, Physica Rapid Research Ltrs 14 (2020) 1900708, https://doi.org/10.1002/pssr.201900708.

[60] S. Ruhle, Tabulated values of the Shockley–Queisser limit for single junction solar cells, Sol. Energy 130 (2016) 139–147, https://doi.org/10.1016/j.solener.2016.02.015.

[61] A. Ruiz-Perona, Y. Sanchez, M. Guc, S. Khelifi, T. Kodalle, M. Placidi, J.M. Merino, M. Leon, R. Caballero, E′ ffect of Na and the back contact on Cu2Zn(Sn,Ge)Se4 thin-film solar cells: towards semi-transparent solar cells, Sol. Energy 206 (2020) 555–563, https://doi.org/10.1016/j.solener.2020.06.044.

[62] G.M. Ford, Q. Guo, R. Agrawal, H.W. Hillhouse, Earth abundant element Cu $_2$ Zn (Sn $_{1-x}$ Ge $_x$)S $_4$ nanocrystals for tunable band gap solar cells: 6.8% efficient device fabrication, Chem. Mater 23 (2011) 2626–2629, https://doi.org/10.1021/cm2002836.

[63] T. Schnabel, M. Seboui, A. Bauer, L. Choubrac, L. Arzel, S. Harel, N. Barreau, E. Ahlswede, Evaluation of different buffer materials for solar cells with wide-gap Cu $_2$ ZnGeS $_x$ Se 4-$_x$ absorbers, RSC Adv 7 (2017) 40105–40110, https://doi.org/10.1039/C7RA06438A.

[64] C.J. Hages, N.J. Carter, R. Agrawal, Generalized quantum efficiency analysis for non-ideal solar cells: case of Cu2ZnSnSe4, J. Appl. Phys 119 (2016) 014505, https://doi.org/10.1063/1.4939487.

[65] E. Ojeda-Duran, K. Monfil-Leyva, J. Andrade-Arvizu, I. Becerril-Romero, Y. Sanchez, R. Fonoll-Rubio, M. Guc, Z. Jehl, J. Luna-Lopez, A. Mu′ noz-Zurita, J. Herr̄ andez-de′ La Luz, V. Izquierdo-Roca, M. Placidi, E. Saucedo, CZTS solar cells and the possibility of increasing VOC using evaporated Al2O3 at the CZTS/CdS interface, Sol. Energy 198 (2020) 696–703, https://doi.org/10.1016/j.solener.2020.02.009.

[66] G. Brammertz, T. Kohl, J. De Wild, D.G. Buldu, G. Birant, M. Meuris, J. Poortmans, B. Vermang, Bias-Dependent admittance spectroscopy of thin-film solar cells: experiment and simulation, IEEE J. Photovoltaics 10 (2020) 1102–1111, https://doi.org/10.1109/JPHOTOV.2020.2992350.

[67] T. Kohl, G. Brammertz, J. De Wild, D.G. Buldu, G. Birant, M. Meuris, J. Poortmans, B. Vermang, Bias dependent admittance spectroscopy of thin film solar cells: KF post deposition treatment, accelerated lifetime testing., and their effect on the CVf loss maps, Sol. Energy Mater. Sol. Cell (2021) 231, https://doi.org/10.1016/j.solmat.2021.111289, 111289.

[68] C.J. Hages, N.J. Carter, R. Agrawal, T. Unold, Generalized current-voltage analysis and efficiency limitations in non-ideal solar cells: case of Cu2ZnSn(SxSe1-x)4 and Cu2Zn(SnyGe1y)(SxSe1-x)4, J. Appl. Phys 115 (2014) 234504, https://doi.org/10.1063/1.4882119.

[69] J. Chantana, Y. Kawano, T. Nishimura, A. Mavlonov, T. Minemoto, Impact of Urbach energy on open-circuit voltage deficit of thin-film solar cells, Sol. Energy Mater. Sol. Cell 210 (2020) 110502, https://doi.org/10.1016/j.solmat.2020.110502.